The Astrophysical Journal, 853:40 (14pp), 2018 January 20 https://doi.org/10.3847/1538-4357/aaa3f6

Magnetized Disk Winds in NGC 3783

Keigo Fukumura[1,8], Demosthenes Kazanas[2], Chris Shrader[2,3], Ehud Behar[4], Francesco Tombesi[2,5,6], and Ioannis Contopoulos[7]
[1] Department of Physics and Astronomy, James Madison University, Harrisonburg, VA 22807, USA; fukumukx@jmu.edu
[2] Astrophysics Science Division, NASA/Goddard Space Flight Center, Greenbelt, MD 20771, USA
[3] Catholic University of America, Washington, DC 20064, USA
[4] Department of Physics, Technion, Haifa 32000, Israel
[5] Department of Astronomy and CRESST, University of Maryland, College Park, MD 20742, USA
[6] Department of Physics, University of Rome "Tor Vergata," Via della Ricerca Scientifica 1, I-00133 Rome, Italy
[7] Research Center for Astronomy, Academy of Athens, Athens 11527, Greece
Received 2017 October 31; revised 2017 December 17; accepted 2017 December 21; published 2018 January 22

Abstract

We analyze a 900 ks stacked *Chandra*/HETG spectrum of NGC 3783 in the context of magnetically driven accretion-disk wind models in an effort to provide tight constraints on the global conditions of the underlying absorbers. Motivated by the earlier measurements of its absorption measure distribution (AMD) indicating X-ray-absorbing ionic columns that decrease slowly with decreasing ionization parameter, we employ 2D magnetohydrodynamic (MHD) disk wind models to describe the global outflow. We compute its photoionization structure along with the wind kinematic properties, allowing us to further calculate in a self-consistent fashion the shapes of the major X-ray absorption lines. With the wind radial density profile determined by the AMD, the profiles of the ensemble of the observed absorption features are determined by the two global parameters of the MHD wind; i.e., disk inclination $\theta_{\rm obs}$ and wind density normalization n_o. Considering the most significant absorption features in the $\sim$1.8–20 Å range, we show that the MHD wind is best described by $n(r) \sim 6.9 \times 10^{11}(r/r_o)^{-1.15}$ cm^{-3} and $\theta_{\rm obs} = 44°$. We argue that winds launched by X-ray heating or radiation pressure, or even MHD winds but with steeper radial density profiles, are strongly disfavored by data. Considering the properties of Fe *K*-band absorption features (i.e., Fe XXV and Fe XXVI), while typically prominent in the active galactic nucleus X-ray spectra, they appear to be weak in NGC 3783. For the specific parameters of our model obtained by fitting the AMD and the rest of the absorption features, these features are found to be weak, in agreement with observations.

Key words: accretion, accretion disks – galaxies: individual (NGC3783) – galaxies: Seyfert – magnetohydrodynamics (MHD) – methods: numerical

1. Introduction

Ionized outflows are a common feature of active galactic nuclei (AGNs), manifesting themselves as blueshifted absorption spectral lines. Approximately 50%–70% of all Seyfert 1s exhibit such features in their UV spectra and a similar fraction in their X-ray spectra (Crenshaw et al. 2003). The most likely process responsible for the outflowing plasma ionization is photoionization by the AGN ionizing continuum; in this respect, X-rays appear to be of broader utility in probing their properties, since X-ray transitions span a much larger range in photoionization parameter ξ than the UV ones.

X-ray absorption features were discovered first in the *Einstein* quasi-stellar object (QSO) spectra (e.g., Halpern 1984), with more significant detections of K-shell absorption edges due to O VII (0.74 keV) and O VIII (0.87 keV) by *ROSAT* (Nandra & Pounds 1992; Fiore et al. 1993; Nandra et al. 1993; Turner et al. 1993). Later on, the improved spectroscopic capabilities of *ASCA* confirmed the robust presence of these edges in many luminous Seyfert AGNs (e.g., Reynolds et al. 1997; George et al. 1998); attributed to absorption by warm plasmas ($T \sim 10^6$ K), they have since been referred to as warm absorbers (WA). With the much-enhanced spectral resolution and senstitivity of dispersive spectrometers onboard *Chandra* and *XMM-Newton*, it became obvious that there exists a plethora of absorption lines of various charge states of many elements; these span a wide range of ionization parameter $\xi \equiv L_{\rm ion}/(nr^2)$ (e.g., Crenshaw et al. 2003; Blustin et al. 2005; Steenbrugge et al. 2005; McKernan et al. 2007), where $L_{\rm ion}$ is the ionizing (X-ray) luminosity and n is the electron number density at radius r. Their columns lie in the range 10^{20} cm $\lesssim N_{\rm H} \lesssim 10^{22}$ cm^{-2}, their ionization parameters in the range $-1 \lesssim \log \xi \lesssim 4$, their temperatures in the range $10^4 < T < 10^7$, and the exhibit line-of-sight (LoS) velocities of $v/c \lesssim 0.01$ (e.g., Reynolds et al. 1995), implying distances $r \gtrsim 10^4$ Schwarzschild radii, employing the Keplerian association between velocity and radius.

NGC 3783 is a nearby ($z = 0.00976$) bright AGN with a black hole mass of $3 \times 10^7\,M_\odot$ (Peterson et al. 2004); it has been observed with *Chandra*/HETGS a number of times to date since 2000 (Kaspi et al. 2000) and in conjunction with simultaneous observations by *ASCA* and *RXTE* (Kaspi et al. 2001, hereafter K01). It is one of the most intensively monitored Seyfert galaxies for its high-resolution absorption study with a total duration of 900 ks *Chandra* grating data (i.e., five $\sim$170 ks observations and a 56 ks one; Kaspi et al. 2002, hereafter K02). The mean X-ray luminosity in 2–10 keV is $L_X = 3 \times 10^{43}$ erg s^{-1} (K01 and K02). In addition to a series of ionized absorbers in the X-ray, NGC 3783 is also known to exhibit UV absorbers detected with *FUSE* and *HST*/STIS (e.g., Kraemer et al. 2001 and references therein). In particular, K02 conducted an exploratory spectral analysis of the detected

[8] KITP Scholar at UC Santa Barbara (2015–2017).

X-ray absorbers, identifying the physical characteristics of individual ions in the broadband stacked spectrum assuming phenomenological multiple absorption systems. They did not find any correlation of their velocity shifts or FWHMs with ionization potentials. Along similar lines, Krongold et al. (2003; also Netzer et al. 2003) analyzed the same 900 ks *Chandra* grating spectrum with a self-consistent photoionization model, assuming a simple geometry that consists of a central source emitting an ionizing spectral energy distribution (SED) and clouds of gas intercepting our LoS. Employing `cloudy` (version 90.04; Ferland et al. 2013) to obtain the individual clouds' ionization state, they were able to constrain the physical parameters of various ions, i.e., their ionization parameter ξ, column $N_{\rm H}$, outflow velocity v, and internal turbulent velocity $v_{\rm turb}$.

In addition to these *Chandra* observations, NGC 3783 was observed with *XMM-Newton*/EPIC over two complete satellite orbits in 2001 (ID 0112210501 and 0112210201), with a total good exposure of 280 ks with gratings (Behar et al. 2003) and ∼240 ks with CCDs, to study the Fe K-line profile (Reeves et al. 2004). As a part of their spectral analysis, it was found that the highest ionization component present during this epoch is at an ionization of $\log \xi \simeq 3$ and column density of $N_{\rm H} \sim 5 \times 10^{22}\,{\rm cm}^{-2}$ at an estimated distance of $r < 0.1$ pc from the nucleus, while the low-ionization states are many pc away. Gabel et al. (2005) confirmed the large distances of the absorbers (with low densities) by observations of C^{+2} transitions from excited levels. More recently, Mehdipour et al. (2017) conducted a *Swift* monitoring campaign triggering joint observations with *XMM-Newton*, *NuSTAR*, and *HST*/COS/STIS in cases of hard *Swift*-XRT spectra, indicating soft X-ray absorption. It was found, in contrast to the previous analyses performed in the 2000–2001 (unobscured) epoch, that the central X-ray region was heavily obscured by outflowing plasma that, besides absorbing the low-energy ($E \lesssim 1\,{\rm keV}$) X-rays, also exhibited deep absorption features very distinct from the absorbers detected in the previous UV/X-ray observations. In particular, high-velocity Fe XXV and Fe XXVI absorbers ($v_{\rm out}\sim$ a few thousand km s^{-1}) of high column density ($N_{\rm H} \sim 10^{23}\,{\rm cm}^{-2}$) are clearly present. While comprehensive in their analysis methodology, the physical realization of the series of absorbers observed was still unclear, consisting of multiple absorber components, as has been often invoked, and the global identification of the observed outflows of many ions is not explicitly revealed.

The presence of ionic species in absorption in the AGN spectra with a broad range in ionization parameter ξ has been generally dealt with by considering a number of separate components of well-defined ξ. An altogether different (and profitable) approach has been that of Holczer et al. (2007); these authors, noticing the broad range in ξ of the ionic species in the data, assumed a continuous distribution of hydrogen-equivalent ionic columns $N_{\rm H}$ on ξ of the form $N_{\rm H} \propto \xi^{\alpha}$ (or, more precisely, the distribution of $dN_{\rm H}/d\log\xi$, their so-called absorption measure distribution (AMD), as discussed below in Equations (1)–(2)). Then, through a minimization procedure, they were able to consolidate the ensemble of the properties of all transitions into the value of a single parameter, namely α, which, surprisingly, was found to have a very limited range $\alpha \simeq 0.01$–0.3 in the number of AGNs with data of sufficiently high quality for such an analysis (Behar 2009, hereafter B09). This behavior has since been found in a joint analysis of 26 Seyfert outflows (Laha et al. 2014).

While the largest possible location $R_{\rm max}$ of an absorber can be estimated by $R_{\rm max} = L_{\rm ion}/(\xi N_{\rm H})$, by recasting the ionization parameter in a slightly different form based on the LoS-integrated hydrogen number density, one can derive a simple analytic expression for a local finite column density $\Delta N_{\rm H}$ for a finite ionization parameter bin $\Delta\xi$ over a small radial LoS extent Δr as

$$\Delta N_{\rm H} = n(r)\Delta r \propto \xi^{(3-2p)/(p-2)}\Delta\xi, \tag{1}$$

where $n(r) \propto r^{-p}$ is the global wind density profile along an LoS. One can then derive the expected AMD as a function of ξ as

$${\rm AMD} \equiv \lim_{\Delta r\to 0}\frac{\Delta N_{\rm H}}{\Delta(\log\xi)} \propto \xi^{-(p-1)/(p-2)}, \tag{2}$$

as similarly derived in B09 and Kazanas et al. (2012). One should note that, for a continuous distribution of $N_{\rm H}$ on ξ, the measurement of the $N_{\rm H}$ of an ion of known ξ provides a measure of its distance r from the ionizing source; repeating this process for ions of a wide range of ξ can then provide the distribution of plasma density $n(r)$ along the observer's LoS. Thus, the observed slope of AMD implies plasma radial density profiles with a rather limited range in their slopes, namely $1.02 \lesssim p \lesssim 1.22$ (see B09 for five Seyfert 1 AGNs, including NGC 3783).

Motivated by these considerations, we have in the past modeled the AMD observations within the framework of the 2D magnetohydrodynamic (MHD) winds of Contopoulos & Lovelace (1994, hereafter CL94), generalizations of those of Blandford & Payne (1982, hereafter BP82), that allow a wider range of wind density profile along the LoS. We found that detailed treatment of the photoionization of MHD winds with $p \simeq 1$ presented a good approximation to the observed AMD dependence and velocity properties of the Seyfert 1s in the list of B09 (Fukumura et al. 2010a, hereafter F10a); we also found that reduction of the ionizing X-ray content in the AGN SED, as is appropriate with the broad absorption line (BAL) QSO spectra, provided velocities consistent with those observed in this AGN class (Fukumura et al. 2010b). Furthermore, considering that our 2D MHD winds are scale invariant (Kazanas et al. 2012), we have applied the same models to the high signal-to-noise ratio (S/N) *Chandra* spectra of the galactic X-ray binary (XRB) GRO J1655-40 (Fukumura et al. 2017) to show that our models provide excellent fits to the absorption features (both in absorption depth and in velocity) of the scaled-down wind of this stellar black hole. In the context of a mutual interaction between accretion and ejection physics, for example, other groups have also investigated a physical constraint on a global structure of MHD-driven outflows (e.g., Ferreira 1997; Casse & Ferreira 2000a, 2000b; Chakravorty et al. 2016).

In the present work, we employ the same 2D MHD wind model as in our previous works to analyze the 900 ks *Chandra* HETG data of NGC 3783, a well-studied, nearby, radio-quiet AGN. With its AMD already determined in B09, our emphasis is the precise determination of the large-scale wind parameters, namely the value of the index p, its inclination angle, and the wind density normalization. This we do by providing detailed fits to its most significant absorption lines. In Section 2, we

provide a brief outline of the MHD winds and a comparison with other outflow models. In Section 3, we describe our analysis procedure. Our results and their comparison to observations are shown in Section 4, demonstrating that the wind model can describe the observations successfully. We summarize and discuss the implications of the model in Section 5.

2. Overview of MHD-driven Wind Model

Given the large bolometric luminosity of AGNs and the X-ray contribution to their continua, it is natural to consider radiation pressure (Murray et al. 1995; Proga et al. 2000) and/or X-ray heating (Begelman et al. 1983) as the agents that drive their ubiquitous outflows. While one cannot give a preference to MHD launching over these processes a priori, the general argument in favor of the latter and against the simplest versions of the former comes from the form of AMD: for both of these processes (i.e., radiation pressure and X-ray heating), at some distance a few times larger than the size of their driving source, these winds will look quasi-spherical, with their velocity increasing with r to its asymptotic value. Then, in their acceleration region ($dv/dr > 0$), due to mass conservation, their densities should decrease faster than r^{-2}, resulting in $N_{\rm H}$ decreasing with increasing ξ (Luketic et al. 2010). Such a behavior is contrary to that observed in the compilation of B09 and Laha et al. (2014). Perhaps more involved models could reproduce the observed $N_{\rm H}$–ξ behavior; however, we are not aware of any so far.

On the other hand, the broad range of ξ observed in the data suggests a self-similar process that spans several decades in ξ and r. The 2D winds of BP82 and CL94 serve as a reasonable guess to this end, as they are launched over the entire disk extent. Their velocities (radial and azimuthal) scale with the Keplerian one, $v_{\rm out} \propto r^{-1/2}$. Their densities are separable in r and θ (due to self-similarity) and take the form $n(r, \theta) = n_o (r/r_S)^{-p} f(\theta)$, where n_o denotes the density normalization (i.e., wind density at its innermost launching radius on the disk surface at $r \gtrsim r_S$, where r_S is the black hole Schwarzschild radius). It can be expressed in units of dimensionless mass flux rate $\dot{m} = \dot{M}/\dot{M}_{\rm Edd}$ by

$$n_o \sim \dot{m}/(\sigma_T r_S), \tag{3}$$

where we assume that accreting mass is equally distributed between accretion and outflows at each radius (i.e., $f_w = 1$ as in F10a; Fukumura et al. 2017). The function $f(\theta)$ determines the angular dependence of the wind, and it is given by the solution of the Grad–Shafranov equation (see CL94). It has a steep θ dependence (an approximate expression is $f(\theta) \sim e^{5(\theta-\pi/2)}$; see Figure 2 of F10a), giving the winds a toroidal appearance. Because of this feature, it was suggested (Königl & Kartje 1994) that such winds are in fact the AGN tori invoked to account for AGN unification. The precise form of $f(\theta)$, i.e., the winds' opening angle, depends on their specific angular momentum (Fukumura et al. 2014). However, it is qualitatively similar to the form given above.

More importantly, the density radial dependence index p above is intimately related to the AMD shape by Equation (2). The wind velocity, mainly in the ϕ direction as $\theta \to 90°$, becomes mainly radial at larger latitudes (see Figure 1(a) in F10a). Its projection along the observer's LoS depends on the disk inclination and affects the shape of absorption features; however, due to their Keplerian scaling, the outflow velocity component scales with ionization parameter ξ like

$$v_{\rm out} \propto \xi^{1/\{2(2-p)\}}, \tag{4}$$

a feature that figures prominently in the shapes of the absorption-line profiles (see F10a and Section 4.1).

The winds have the following generic features. (1) The wind structure (i.e., the dependence of $N_{\rm H}$ on θ and r/r_S) is fundamentally mass invariant, so it is applicable across the black hole mass scales. (2) They extend from near the black hole innermost stable circular orbit (ISCO; $r \gtrsim 3\, r_S$) to the outer disk edge, with velocities that decrease like $r^{-1/2}$. The first feature is indicative of the universal presence of magnetically launched ionized winds in both AGNs (e.g., Couto et al. 2016; Kraemer et al. 2018 for NGC 4151 and Turner et al. 2005 for NGC 3516) and XRBs, as often claimed (e.g., Miller et al. 2006, 2008, 2015; Kallman et al. 2009; Fukumura et al. 2017). The second feature clearly points to a strong relevance to the so-called ultra-fast outflows (UFOs), increasingly discovered in many Seyfert AGNs (e.g., Reeves et al. 2009; Tombesi et al. 2010, 2013, 2015; Gofford et al. 2015; Gupta et al. 2015) and gravitationally lensed quasars (e.g., Chartas et al. 2009b), and their relation to the lower-velocity WAs. Especially, Kraemer et al. (2018) made a strong argument to support the MHD-driven scenario to explain the UFOs detected in NGC 4151 in an approach similar to ours. As noted above, while the wind is present at all radii and their corresponding velocities, its full ionization in the black hole vicinity leaves no absorption imprints in the spectra. These first occur when the wind ionization drops sufficiently to allow the presence of Fe XXVI and Fe XXV; the radii at which these ions first occur depend on the contribution of the ionizing X-rays in the object's SED. The radii are small in X-ray-weak (BAL QSOs) and large in X-ray-strong (galactic XRBs) objects, yielding correspondingly large and small velocities for these ions.

The wind photoionization is computed as detailed in F10a by employing `xstar` (Kallman & Bautista 2001) to determine the plasma ionization and the relevant cross sections to be used in the radiation transfer. Finally, we compute absorption-line profiles by calculating the photoexcitation cross section

$$\sigma_{\rm abs} = 0.01495 (f_{ij}/\Delta\nu_D) H(a, u) \tag{5}$$

as a function of local wind velocity $v(r, \theta)$ and its radial shear $\Delta v_{\rm sh}(r, \theta)$ through the Voigt function $H(a, u)$, where f_{ij} is the oscillator strength of the transition between the ith and jth levels of an ionic species and $\Delta\nu_D$ is the Doppler broadening factor estimated by $\Delta\nu_D \approx (\Delta v_{\rm sh}/c)\nu_0$ relative to the centroid (rest-frame) frequency ν_0. With $\sigma_{\rm abs}$ in Equation (5), one can calculate the line depth τ as

$$\tau = \sigma_{\rm abs} N_{\rm ion}, \tag{6}$$

where $N_{\rm ion}$ is ionic column density computed with `xstar` calculations (see, e.g., Fukumura et al. 2015). In this formalism, therefore, the line broadening is provided by the natural shear of the wind velocity field, and, as such, we eschew the use of the turbulent velocity parameter `vturb`; most importantly, all line profiles are computed using the local values ofthe same global wind parameters rather than being treated as mutually independent multiple Gaussian functions, thereby overconstraining our models.

3. Analysis

For the present study, we use the 900 ks stacked spectrum from K02 (see their Figure 5). Our analysis is primarily focused on the ∼1 Å (Fe)–20 Å (O) broadband spectral fitting with the Galactic absorption of $N_{\rm H}^{\rm Gal} = 8.7 \times 10^{20}$ cm^{-2} (e.g., Alloin et al. 1995). Closely following K01 and K02, we estimate the underlying continuum flux in discrete energy bands where few or no line signatures are present (i.e., line-free zones (LFZs)). The continuum spectral shape is assumed to be locally linear instead of a polynomial form, which seems to be quite acceptable, as also claimed in K02, our aim in the present work not being a physical model of the AGN continuum. Contrary to most works, which assume a mutually decoupled, discrete number of ionization and kinematic components to fit groups of lines of similar values of ξ, our models provide a continuum of ionization parameter, column, and velocity projection along the LoS with r, the distance from the AGN. As a result, our models are far more constrained, with no guarantee that they will provide the correct column equivalent width (EW) and velocity at the proper values of ξ that support specific ions.

Our investigation begins with calculating the structure of various magnetized wind solutions of different global density profiles that essentially determine the absorber's AMD. Specifically, we consider $p = 1.29$, 1.15, 1, 0.9, 0.8, and 0.7, consistent with the relevant range obtained in B09 for NGC 3783. For photoionization calculations with `xstar`, we adopt the same ionizing SED of NGC 3783 as determined in K01 (see their Table 4) by the LFZ continuum fitting, i.e., a composite spectrum of multiple power-law components of different slopes between 0.2 eV and 30 keV, namely $\Gamma = 2.0$ (0.2–2 eV), 1.5 (2–40 eV), 5.77 (40 eV–0.1 keV), and 1.77 (0.1–30 keV). We adopt the ionizing luminosity, $L_X = 3 \times 10^{43}$ erg s^{-1}, in 1–1000 Ry (see, e.g., K01 and K02) for the photoionization calculations. The AGN SED is generally broadband, covering wavelengths much broader than the X-rays. However, UV photons of energy below 1 Ry (13.6 eV, the threshold energy for ionizing hydrogen) do not contribute to the photoionization of the wind, while harder X-ray photons of energy higher than 1000 Ry (13.6 keV) typically have much lower flux (compared to that of soft X-rays) and do not make a significant impact on the overall photoionization process. The broader disk SED photons emitted near the black hole ($r \gtrsim r_o$) contribute to the cooling of the ionized gas, and those have been included in our calculations.

This SED is injected at the coordinate origin as an irradiating source, mimicking the compact point source of an X-ray corona. As mentioned, a given SED will uniquely determine the ionization structure of the wind that "breaks" the otherwise mass-invariant spatial nature of the MHD-driven X-ray absorbers. To show the predictive power of our models, Figure 1 shows, as one of many (typically 12–15) template calculations, a synthetic AMD for a number of ions computed with $p = 1.15$ wind for $\theta_{\rm obs} = 40°$ and $n_{11} = 13.6$, where $n_o \equiv n_{11} 10^{11}\,{\rm cm}^{-3}$. As seen, the peak column of a given ion increases with ionization parameter ξ (and with decreasing distance r), and the slope of this AMD (=0.176 from Equation (2); dashed line), consistent with that derived in B09, is set by the wind density slope of $p = 1.15$, assuming the solar abundances. The LoS wind velocity scales as Keplerian, $r^{-1/2}$, in this model.

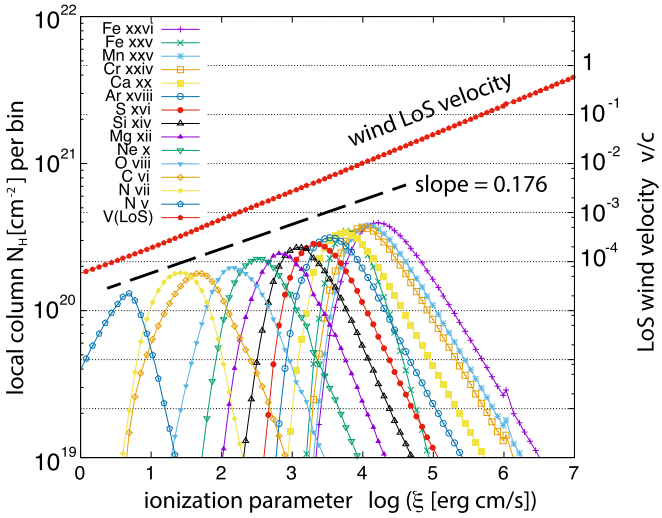

Figure 1. Example of synthetic AMD of various ions modeled with the MHD wind of density profile $p = 1.15$ for a fiducial set of wind parameters with $\theta = 40°$ and $n_{11} = 13.6$.

In our investigation, 18 absorption lines (see Tables 2–3 and Figures 2–3, which will be discussed more in Section 4) are modeled systematically and globally, in the sense that they are all computed within the confines of a single, continuous disk wind. This can pose tight restrictions on the model, since, in such a global model, we cannot afford to adjust individual absorber parameters independently to obtain good fits for specific features. As a result, for a given density distribution p (obtained by spectral fitting and AMD), our model has only two free parameters: (1) the wind density normalization n_o at the innermost launching radius at $r \gtrsim r_S$ on the disk surface and (2) the disk inclination angle $\theta_{\rm obs}$. Elemental abundances could be adjusted individually, but solar abundances are assumed here. Finally, considering that the observed spectrum also exhibits a number of prominent emission lines, especially toward longer wavelengths, we have added, as needed, emission features to our model continuum spectrum of the EW derived in K02.

First, we try to narrow down an optimal range of model parameters by crudely exploring the parameter space spanned by (n_{11}, $\theta_{\rm obs}$) for a series of wind density structure given by p, where n_{11} is defined as $n_o \equiv n_{11} 10^{11}$ cm^{-3}. The likely value of p is successfully constrained within the error set by B09 and Laha et al. (2014). Following this preliminary investigation, a primary grid of models is determined, as shown in Table 1. A more thorough analysis is then conducted for these template models to compute in addition the physical parameters of individual ions (e.g., distance r, column $N_{\rm H}$, number density n, velocity $v_{\rm out}$, ionization parameter ξ, plasma temperature T); this is done for the major spectral signatures for a total of 18 transition lines from major H/He-like ions, i.e., Fe, Ar, S, Si, Mg, Al, Ne, O, and N of relatively large EWs found in K02 over the ∼1–20 Å band, as they present the most significant indicators of the best-fit global wind solution.

4. Results

To quantitatively assess the model's statistical significance, we create a large number (typically 12–15) of template wind solutions with different sets of (n_{11}, $\theta_{\rm obs}$), where $0.1 \leqslant n_{11} \leqslant 100$ and $30° \leqslant \theta_{\rm obs} \leqslant 60°$ for a given p within the relevant range

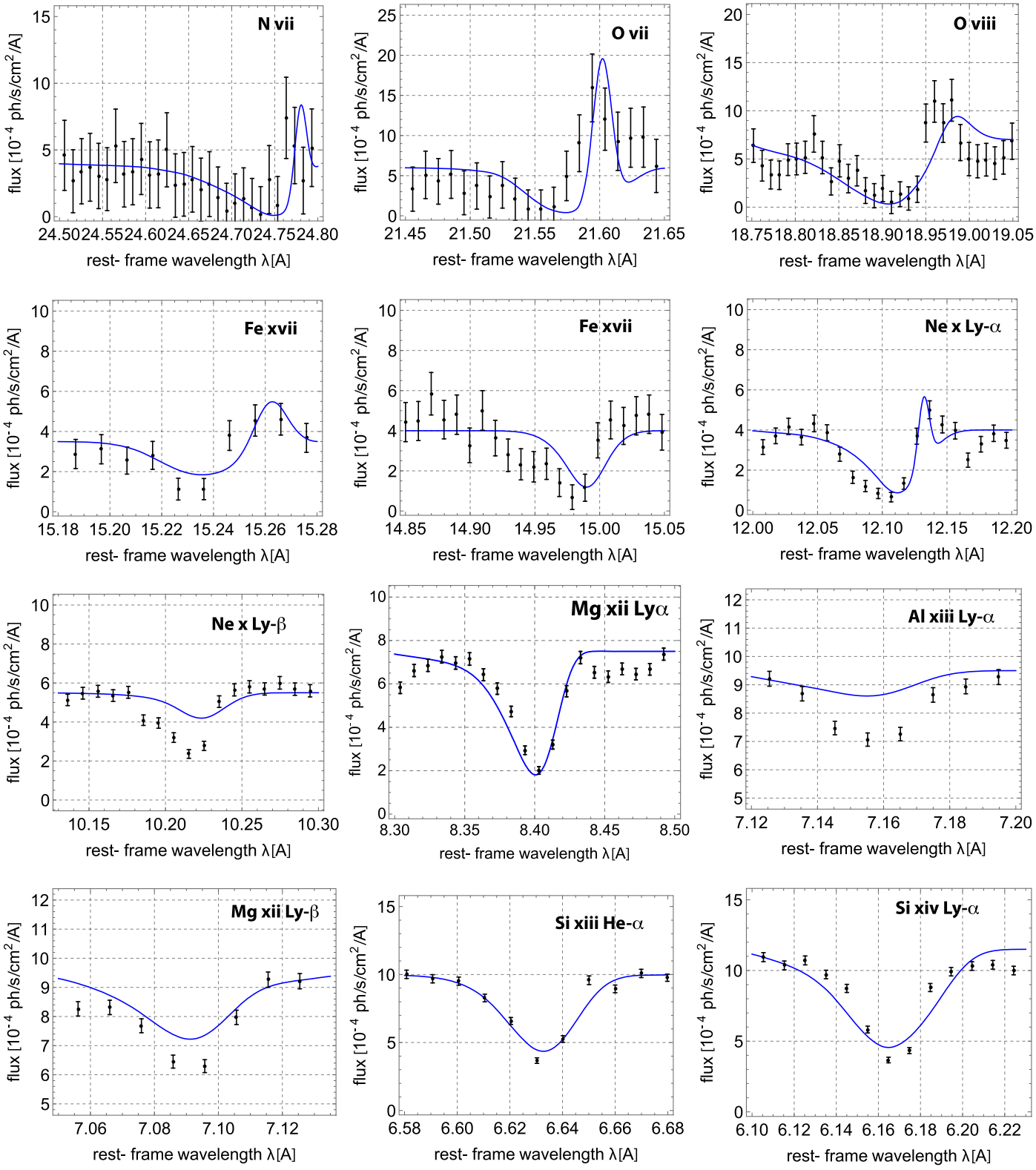

Figure 2. Sample of the best-fit spectra calculated from the modeled MHD wind (blue lines) with $p = 1.15$, $\theta_{\rm obs} = 44°$, and $n_{11} = 6.9$. See Tables 2 and 3 for more details.

inferred from B09, as shown in Table 1. For each such pair of (n_{11}, $\theta_{\rm obs}$), we compute the predominantly strong absorption-line profiles and calculate the χ^2/dof from the ensemble of 18 absorption lines. Minimization of χ^2 for each density profile yields the best-fit spectrum solution, and we calculate the EW for each transition line both from our wind model and from the data. Besides the value of χ^2, we also calculate a ratio as another useful proxy for goodness-of-fit, $R_{\rm EW} \equiv {\rm EW(obs)/EW(model)}$, of the observed to the model EW for each ion. In Figure 4, we plot the ratios $R_{\rm EW}$ as a function of atomic number Z along with

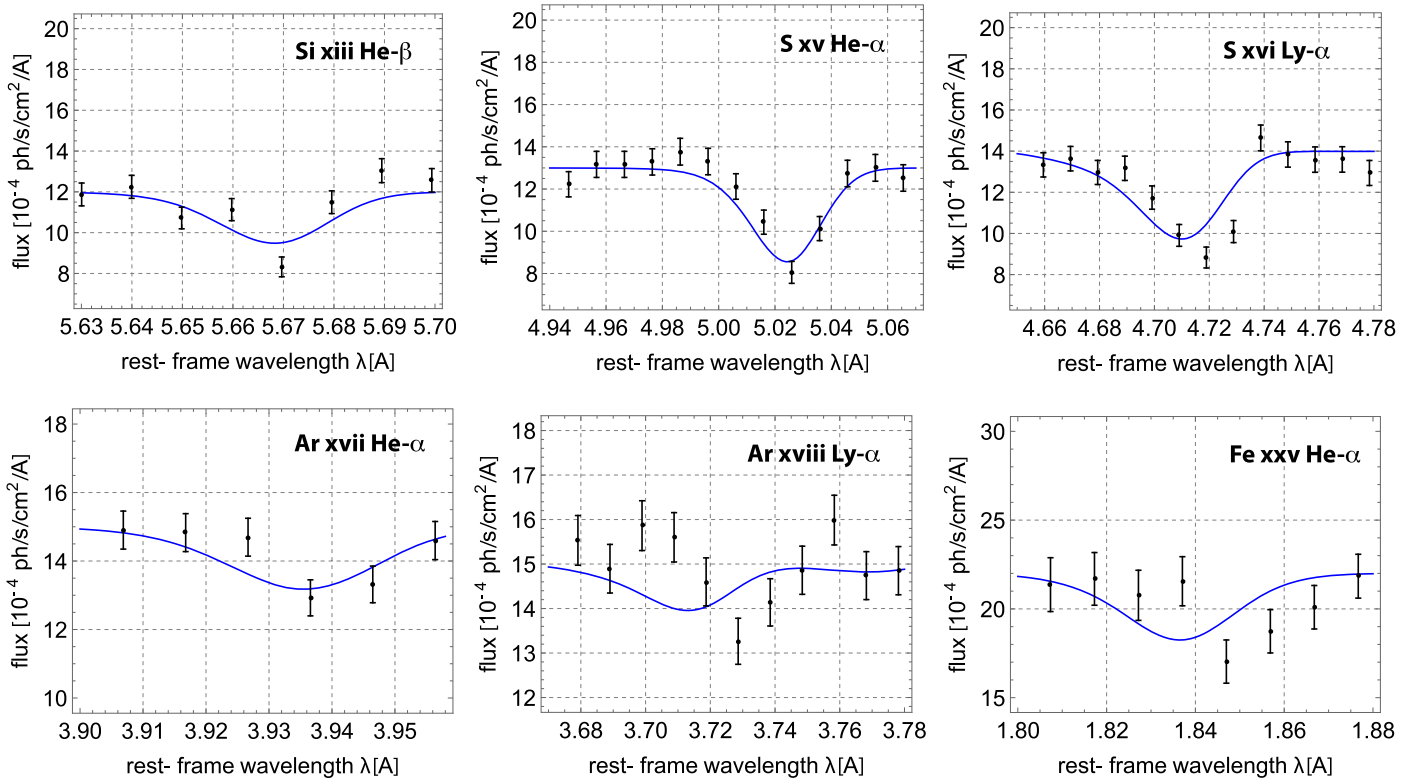

Figure 3. Sample of the best-fit spectra calculated from the modeled MHD wind (blue lines) with $p = 1.15$, $\theta_{\rm obs} = 44°$, and $n_{11} = 6.9$. See Tables 2 and 3 for more details.

Table 1
Primary Grid of MHD Wind Model Parameters

Primary Parameter	Value
Wind density slope p	0.7, 0.8, 0.9, 1.0, 1.15, 1.29
Inclination angle θ [deg]	30°, 40°, 50°
Wind density normalization n_{11}[a]	0.1−100

Note. We assume $M = 3 \times 10^7\,M_\odot$ (Peterson et al. 2004) and $L_X = 3 \times 10^{43}$ erg s^{-1} (K02).
[a] Wind density normalization in units of 10^{11} cm^{-3}.

their mean value $\bar{R}_{\rm EW}$ (red lines). The inset of each panel denotes the resulting value of $\bar{R}_{\rm EW}$ along with the corresponding χ^2/dof values for the specific value of p. Assuming that the wind characteristics vary monotonically with the wind density parameter p, it is implied here that the global best-fit solution spanned by the (n_{11}, $\theta_{\rm obs}$; p) space is found somewhere around $p = 1.15$, which is in fact consistent with the result from B09.

To better illustrate the goodness-of-fit in our spectral analysis, we plot in Figure 5(a) the values of $100(\bar{R}_{\rm EW} - 1)$ (black circles with line) and the corresponding χ^2/dof values (red triangles with line) as a function of the value p. We do see that the χ^2 statistics is rather insensitive to the value of $0.8 \lesssim p \lesssim 1.15$ but increases steeply outside this range. It should be noted here that the χ^2 statistics in this data set is predominantly controlled by a small number of stronger lines with very small error bars produced around $\xi \sim 2.5$. As long as the choice of a pair of (n_{11}, $\theta_{\rm obs}$) produces the correct value of column density at the given value of ξ, the model gives a similarly small χ^2/dof value. However, it fails here at higher values of ξ because not many high-Z elements are detected with large significance in these data. On the other hand, the EW ratios $\bar{R}_{\rm EW}$ fare better in that respect, as they provide an alternative to the AMD covering a larger ξ range. From the combination of the two proxies here, we see again that p in the range ∼1–1.15 provides the most satisfactory fit to the data. The most likely ranges from our best fit (labeled *MHD Wind*) and the AMD in B09 (labeled *AMD*) are denoted by shaded regions. In the remainder of this paper, therefore, we choose the value $p = 1.15$ as the best-fit wind solution from a global perspective. For $p = 1.15$, we also present in Figure 5(b) a contour map of χ^2/dof (color-coded as shown) in the $\theta_{\rm obs}$–n_{11} plane to obtain the best-fit solution of $\theta \simeq 44°$ and $n_{11} \simeq 6.9$ (denoted by a cross).

Focused on the obtained global best-fit solution, we presented earlier in Figures 2–3 the best-fit profiles of the 18 lines of Table 2 with $p = 1.15$, $\theta_{\rm obs} = 44°$, and $n_{11} = 6.9$ (i.e., $n_o = 6.9 \times 10^{11}$ cm^{-3}) overlaid on the data. Note that our spectral calculations employ the Voigt profile as described above, with the wind shear as the only line-broadening process, eschewing the use of an artificial turbulent velocity, customarily employed in similar analyses. This set of wind parameters is statistically favored among the models considered here (as demonstrated in Figure 5). As also seen in Figures 2 and 3, the global best-fit model (i.e., $p = 1.15$ wind) is generally consistent with most significant absorber transitions, both in line depth and in shape (the Ne X Lyβ feature may involve line blending, not considered here). As discussed elsewhere in this paper, the Fe XXV Heα line, typically strong in the AGN absorption spectra (Tombesi et al. 2013), is rather weak in this object, in agreement with our model, lending additional support to it.

Besides the observable quantities discussed so far (as listed in Table 2), we also calculate the characteristics associated with

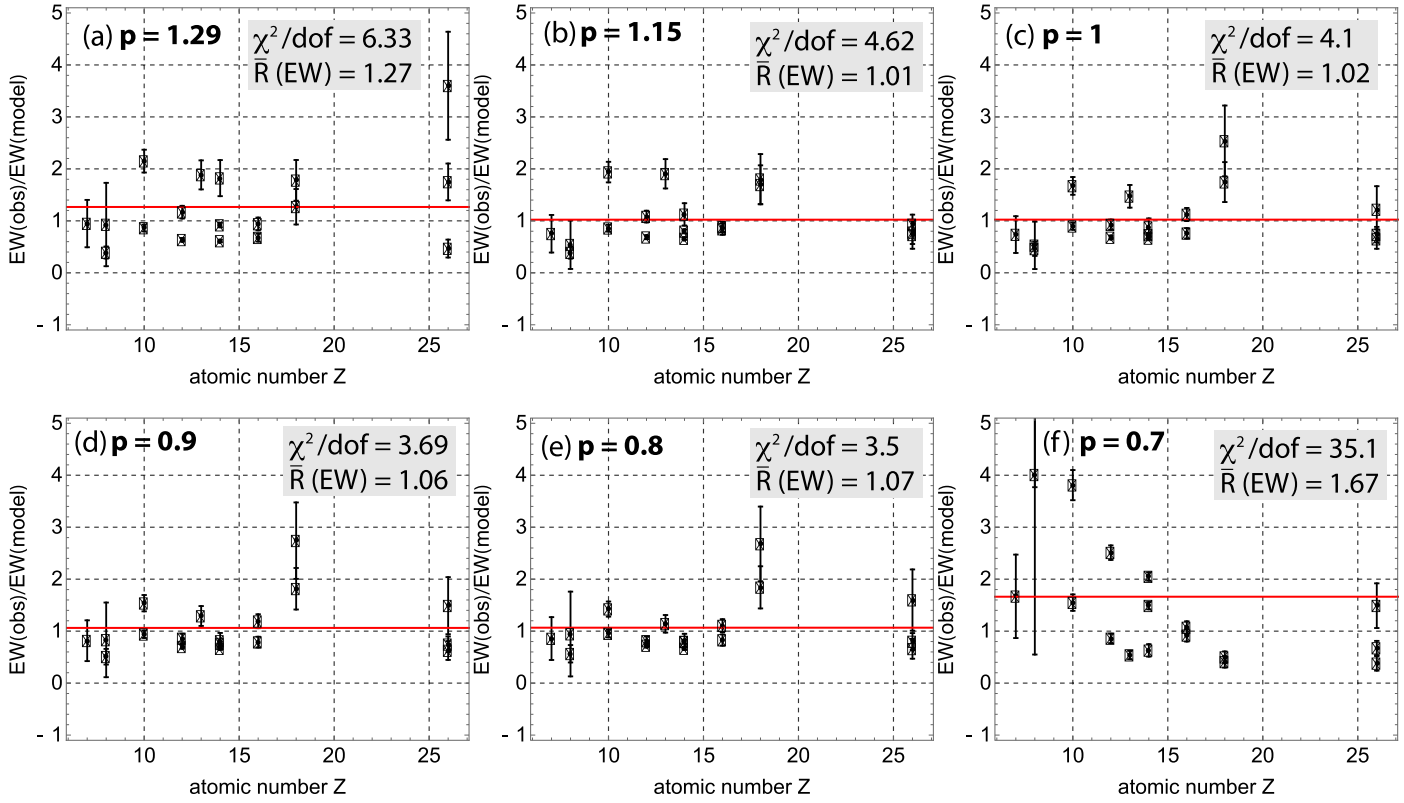

Figure 4. EW ratios, $R_{\rm EW}\equiv$ EW(obs)/EW(model), between the model and observation for the same 18 ions shown in Table 2 derived from the best-fit models for various wind density profiles, (a) $p = 1.29$, (b) 1.15, (c) 1.0, (d) 0.9, (e) 0.8, and (f) 0.7, along with its mean value, $\bar{R}_{\rm EW}$ (red lines). Also shown are the derived χ^2/dof values for each best-fit model from the 18 ions in Table 2. As seen, the $p = 1.0$–1.15 wind is physically more favored at a statistically significant level.

specific lines of our magnetically driven disk winds. Representative wind variables are listed in Table 3 in order of increasing characteristic LoS distance, r_c (third column), where the local ionic column obtains its maximum value for each line. We also show the local wind density n_c (sixth column) and line optical depth τ_c (eighth column) at this characteristic radius r_c. Accordingly, we keep track of the radial dynamic range over which the local ionic column stays within 50% of its maximum value. Within this range, the ionization parameter ξ (fourth column) and the wind temperature T (fifth column) are computed as well. Lastly, the LoS-integrated hydrogen-equivalent column density of each ion $N_{\rm H}^{\rm tot}$ is also calculated (seventh column). As shown, the distances of absorbers range from 0.2 to 30 pc scales in X-rays, exactly as estimated for this source by Behar et al. (2003), Reeves et al. (2004), and Gabel et al. (2005). In most of the radial extent of the wind, absorbers are optically thin where the radiative transfer calculations with `xstar` are justified.

It should be remembered that continuous outflows are characterized, in general, by a gradient of the wind's physical quantities (e.g., density, velocity, etc.), a situation fundamentally distinct from outflow models consisting of distinct, independent, multiple kinematic and ionization components. In the continuous outflow situation, all wind elements leave their imprint on the line profile at their respective velocities, weighted, of course, by the corresponding ionic abundance. For example, in the specific wind structure considered here, the ionic abundances are not symmetric with respect to the value of ξ where they achieve their maximum; they fall much sharper at lower ξ values (and lower velocities) than at higher ones (higher velocities; see one of the template AMDs as shown in Figure 1). As a result, the resulting absorption lines are asymmetric, skewed toward their blue side, and their peak absorption is at a velocity larger than that corresponding to their peak column (see Section 4.1 below).

4.1. The $v_{\rm out}$–ξ Correlation

The continuous variation of ξ and outflow velocity $v_{\rm out}$ with distance r implies a correlation between ξ and the projected outflow velocity along the observer's LoS $v_{\rm out}$ (i.e., Equation (4)). Such a relation has been searched empirically in the data. For example, Detmers et al. (2011) found the correlation $v_{\rm out}\propto\xi^{0.64\pm0.1}$ in the data of the 600 ks *XMM-Newton*/RGS multiwavelength campaign of Mrk 509 roughly consistent with our scaling value in Equation (3) for $p = 1.15$. Tombesi et al. (2013) conducted a systematic analysis of the observed WAs and UFOs from a sample of 35 Seyfert 1 galaxies and found that $v_{\rm out}\propto\xi^{0.65}$ for the WAs and UFOs combined together, while $v_{\rm out}\propto\xi^{0.31}$ for the WAs only (see also Laha et al. 2014 for a similar analysis).

However, before strong conclusions are drawn, one should first bear in mind that all the points shown in Tombesi et al. (2013) represent data from a large number of AGNs of different inclinations, columns, and SEDs. The derived scaling law, Equation (4), appears to be generic, but it should be remembered (as mentioned elsewhere in this paper) that the magnetic field and velocity structure of our model winds are self-similar, laterally stacked paraboloids, while the ionizing radiation (at least in our calculations so far) is spherically symmetric about the AGN. Therefore, deviations from the generic relation of Equation (4) should not be surprising in a more detailed modeling.

Table 2
Line Measurements and Best-fit Model for 18 Absorbers

#	Ion	Wavelength[a]	EW(mod)[b]	EW(obs)[b]	$v_{\rm out}^{\rm obs}/v_{\rm out}^{\rm mod}$ [c]	EW(obs)/EW(mod)
1	Fe XXV Heα	1.8505	5.18	3.8 ± 1.4	571/2187	0.73 ± 0.27
2	Ar XVIII Lyα	3.7310	2.28	4.1 ± 1.1	192/1446	1.8 ± 0.48
3	Ar XVII Heα	3.9493	2.94	5.0 ± 1.1	965/1009	1.69 ± 0.37
4	S XVI Lyα	4.7274	12.1	10.7 ± 1.2	536/1103	0.88 ± 0.09
5	S XV Heα	5.0387	10.9	9.2 ± 1.2	759/874	0.84 ± 0.11
6	Si XIII Heβ	5.6807	5.59	6.30 ± 1.2	582/670	1.12 ± 0.21
7	Si XIV Lyα	6.1804	31.0	20.5 ± 0.8	755/747	0.66 ± 0.025
8	Si XIII Heα	6.6480	18.6	14.9 ± 0.7	798/676	0.79 ± 0.04
9	Mg XII Lyβ	7.1058	7.95	8.60 ± 0.9	424/624	1.1 ± 0.11
10	Al XIII Lyα	7.1763	2.83	5.4 ± 0.8	883/890	1.9 ± 0.28
11	Mg XII Lyα	8.4192	36.6	25.1 ± 1.4	577/683	0.69 ± 0.04
12	Ne X Lyβ	10.238	10.1	19.6 ± 2.0	664/439	1.9 ± 0.19
13	Ne X Lyα	12.132	44.3	38.1 ± 2.9	622/494	0.86 ± 0.065
14	Fe XVII	15.014	28.2	26.2 ± 5.3	623/399	0.93 ± 0.18
15	Fe XVII	15.262	19.1	14.9 ± 4.3	699/510	0.78 ± 0.22
16	O VIIILyα	18.969	137	53.6 ± 15.9	925/742	0.38 ± 0.11
17	O VII Heα	21.602	74.1	40.1 ± 34.6	629/333	0.54 ± 0.46
18	N VII Lyα	24.781	96.5	72.6 ± 34.9	573/387	0.75 ± 0.36

Notes.
[a] In units of Å.
[b] In units of mÅ taken from Kaspi et al. (2002).
[c] Velocities in units of km s^{-1}.

Figure 6(a) depicts such $v_{\rm out}$–ξ correlations based on two different standpoints. The triangles represent the correlation of ion velocity $v_{\rm out}$ with the value of ξ at a characteristic radius, r_c (see Table 3), where each ion achieves its maximum column density by photoionization along the LoS (see Figure 1). These points are indeed in excellent agreement with the expected relation of Equation (4) of a slope of 0.58 (red line) for the best-fit $p = 1.15$ wind. However, the line optical depth $\tau_{\rm ion}$ may not necessarily be the greatest at $r = r_c$, as the photoabsorption cross section $\sigma_{\rm abs}$ given by Equation (5) is monotonically increasing with distance, causing the peak of the line depth to shift slightly outward along the LoS. Hence, the outflow velocity derived from the model spectral-line trough is systematically lower than the velocity at $r = r_c$; however, this shift cannot be deduced without detailed line modeling. Thus, as is customary, we use a centroid wavelength to refer to the wind LoS velocity. The results of these measurements based on the line troughs are represented by the circles in Figure 6(a); as already seen in Figures 2 and 3, these data agree well with the expected velocities from the best-fit model. Their velocities appear to be well correlated to the ionization parameter ξ, but its slope is different from the simple analytic prediction of $v_{\rm out} \propto \xi^{1/\{2(2-p)\}}$. The best-fit linear regression yields $v_{\rm out} \propto \xi^{0.37}$ (blue line). This is, in fact, very close to that from the WA ($\simeq$0.31) quoted in Tombesi et al. (2013). One cannot fail to notice that this is much flatter than what one would naively expect from Equation (4).

In summary, one should note that detailed modeling of the line profiles of individual objects is necessary, along the lines of a well-defined model, in order to decide on the implications of the $v_{\rm out}$–ξ correlations of specific observations. We defer general statements on this issue until we have modeled this correlation for a wide range of wind parameters, the subject of a future publication. Finally, one should bear in mind that our models represent a self-similar steady-state model. We do know that AGNs are variable on both short and long timescales. Our models assume that variations in the disk mass flux are also reflected in the mass flux of the wind; these variations are likely to break the simple power-law density profiles assumed so far, producing, for example, increased absorption in earlier, less-absorbed spectra (e.g., Mehdipour et al. 2017). Also, factors other than magnetic fields may influence the wind mass flux; for example, increased mass flux beyond that of self-similarity at the inner wind regions due, e.g., to radiation pressure would produce higher columns for the highest ξ ions, in agreement with the Tombesi et al. (2013) compilation.

5. Discussion and Conclusions

The 900 ks *Chandra*/HETG spectrum of the luminous, radio-quiet Seyfert 1 AGN NGC 3783 is analyzed with an emphasis on its X-ray absorption spectrum, which was modeled within the framework of magnetically driven accretion-disk winds. With its AMD already determined in B09, in conjunction with earlier extensive spectral studies (e.g., K01, K02, and Krongold et al. 2003), we focused on the ~2–20 Å X-ray band to model the properties of its most important transitions in this range. Comparison of the absorber properties to observations, then, provides the global parameters of this wind, namely its density index p, its normalization n_o at its innermost launch radius (of order r_S), and its inclination angle $\theta_{\rm obs}$. Thus, we found, in the context of this model, that the wind radial density profile is given by $n(r) \simeq 6.9 \times 10^{11} (r/r_S)^{-1.15}\,{\rm cm}^{-3}$, along with $\theta \simeq 44°$ for the inclination angle. One should note that the value of the density profile index $p = 1.15$ is consistent with that inferred in B09 and obtained on the basis of the apparent absorption-line column $N_{\rm H}$. However, the present analysis includes additional kinematic information (see Figures 2–3) via mutually coupled ions that affects the shape and EW of the observed lines, features that allow for a refinement of the precise value for p. The

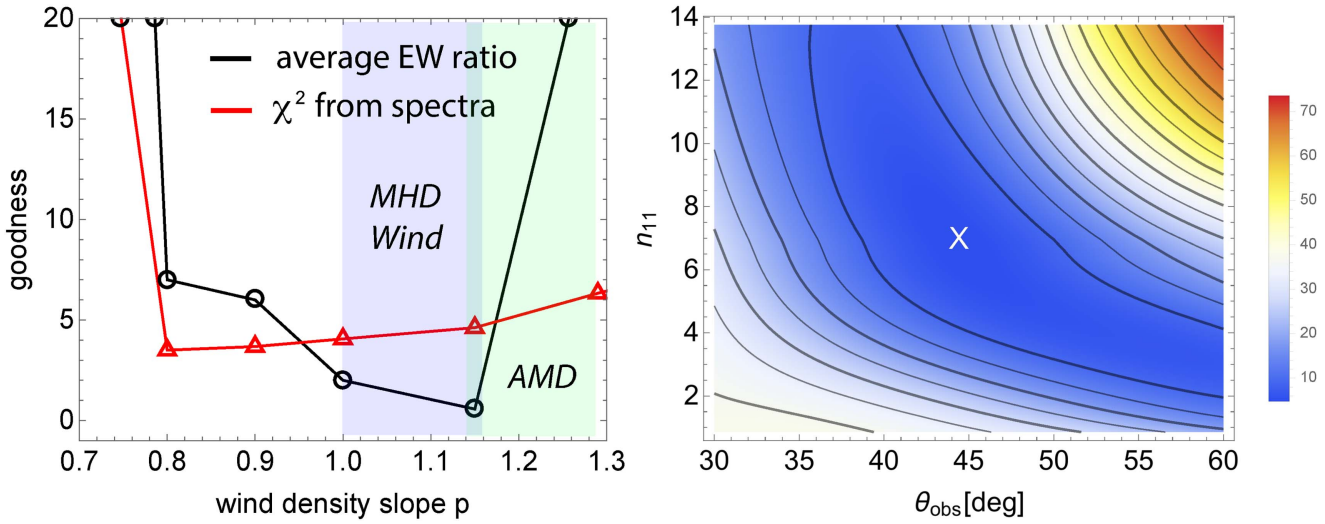

Figure 5. (a) Goodness-of-fit assessed by χ^2 statistics (red triangles) and the mean EW ratios (black circles), $\bar{R}_{\rm EW} \equiv 100(\bar{R} - 1)$, i.e., its percent deviation from a perfect match, corresponding to Figure 4 for the different density slope p considered in this work. The light blue band indicates the most likely values based on the combination of the two constraints. Note that the points for $p = 0.7$ are off the range, as similarly shown in Figure 4. The most likely ranges from our best fit (labeled *MHD Wind*) and the AMD in B09 (labeled *AMD*) are denoted by shaded regions. (b) Contour plot of χ^2/dof values (color-coded) corresponding to the model parameters (n_{11}, $\theta_{\rm obs}$) from the $p = 1.15$ wind with its best-fit solution $\theta = 44^\circ$ and $n_{11} = 6.9$ (cross).

obtained values of (p, n_{11}), as well as the inclination angle $\theta_{\rm obs}$, are determined by fitting the spectroscopic observations assuming a radially self-similar wind model. These constraints are therefore consistent and reasonable with the spectral results.

This is our second application of the specific MHD wind formalism to determine global properties through modeling the multiline absorption X-ray spectra of accreting black holes, our previous analysis being that of the spectrum of the galactic X-ray black hole binary GRO J1655-40 (Fukumura et al. 2017). We have argued elsewhere (e.g., Kazanas et al. 2012) that these models are scale-free and should be applicable to any accreting black holes. We are very encouraged by the ability of this most simple, self-similar model to reproduce the properties of absorption features of outflows associated with objects of such disparate mass scales. In this section, we discuss the results and conclusions of our present analysis and their relation to similar observations of this and other AGNs.

In fact, it has been long speculated that some Seyfert AGNs may exhibit ionized winds whose physical characteristics indeed favor the MHD-driven scenario. For example, Turner et al. (2005) found a series of X-ray absorption lines in *Chandra* grating data and investigated the nature of their physical properties. They argued that some absorbers are too highly ionized to be radiatively accelerated, which can be circumstantial evidence for a hydromagnetic origin for the outflow in NGC 3516. From a synergistic analysis of another well-known Seyfert 1 galaxy, NGC 4151, by Couto et al. (2016), some components of the observed X-ray absorbers are highly ionized. Given the observed 2–10 keV flux and photoionization modeling, the calculated force multiplier is found to be too small to drive the observed winds, perhaps indicating a magnetic origin. These observations may be pointing to the relevance of MHD-driven processes, at least in part if not fully, as discussed in this work for NGC 3783, as well as our earlier work for the XRB GRO J1655-40.

It should be noted that our model treats the underlying accretion disk as a boundary condition that provides the seed plasma for the winds. Hence, accretion and outflows are solved independently. In reality, however, the inflow-outflow problem must be self-consistently considered. Some authors (e.g., Ferreira 1997; Casse & Ferreira 2000a, 2000b; Chakravorty et al. 2016) have attempted this problem by assuming that magnetic flux is brought in from infinity and its advection is balanced by its diffusion. They show that this requirement tends to lead to a very steep density profile of $p \simeq 3/2$, inconsistent with the X-ray AMD observations (e.g., B09), as discussed in this paper. Under a certain ionization parameter space, on the other hand, they argue that a less steep profile ($p \sim 1.1$), as favored in our work here, could be obtained. The qualitative argument for winds such as those considered here is that the viscous torques that transfer the disk angular momentum outward also transfer mechanical energy (and possibly magnetic flux; see Contopoulos et al. 2017). It is this energy that powers the wind mass flux. Although the mutual coupling among inflows, outflows, and threaded magnetic fields is fundamentally important, it is beyond the scope of our current work.

Among the X-ray AGN absorption features, Fe XXV and Fe XXVI have attracted particular attention because of their ubiquity and high velocities, as in the UFOs (Tombesi et al. 2013). These properties have also prompted their study in NGC 3783 by *XMM-Newton* (Reeves et al. 2004). Fits of the broader Fe XXV band with multicomponent, photoionized plasma provide absorber parameters similar to ours. However, in similarity with Mrk 509, the Fe XXV feature is weak in this AGN too. We speculate that this is the result of the relatively low inclination angle and the SEDs in both objects. While systematically consistent for many ions, the observed velocities of high-Z ions, such as Fe and Ar, appear to be lower than what is predicted by the model (i.e., $\sim$1000–2000 km s^{-1}; see Table 2 and Figure 3). As is characteristic of the wind model, heavier absorbers (e.g., Fe) emerge at smaller distances, where the velocities are higher. As a consequence, the resulting absorption features are expected to be broader. There are several ways to account for the discrepancy that may involve all of them. First of all, the error bars of these line transitions are much larger than those of longer wavelengths, making this discrepancy less significant. Second, our calculations have

Table 3
Best-fit Photoionization Modeling for 18 Absorbers

#	Ion	$\log(r_c/r_S)$[a]	$\Delta(\log\xi)$[b]	$\Delta(\log T)$[c]	$\log n_c$[d]	$N_{\rm H}^{\rm tot}$[e]	τ_c
1	Fe XXV Heα	4.96	3.5–4.2	6.0–6.4	6.1	6.1	0.27
2	Ar XVIII Lyα	5.2	3.0–4.1	5.9–6.3	5.8	9.5	0.048
3	Ar XVII Heα	6.7	2.7–3.5	5.8–6.0	5.4	5.7	0.22
4	S XVI Lyα	5.5	2.8–3.9	5.8–6.2	5.5	8.7	0.27
5	S XV Heα	6.0	2.5–3.3	5.7–5.9	4.9	4.6	0.12
6	Si XIII Heβ	6.3	2.2–2.9	5.6–5.8	4.5	4.1	0.76
7	Si XIV Lyα	5.8	2.5–3.7	5.7–6.1	5.1	8.1	1.0
8	Si XIII Heα	6.4	2.2–3.0	5.6–5.9	4.5	4.0	4.4
9	Mg XII Lyβ	6.1	2.3–3.4	5.6–6.0	4.8	4.8	0.27
10	Al XIII Lyα	6.1	2.3–3.4	5.6–6.0	4.8	6.7	0.05
11	Mg XII Lyα	6.1	2.3–3.4	5.6–6.0	4.8	4.8	1.7
12	Ne X Lyβ	6.5	2.0–3.0	5.0–5.8	4.3	4.9	0.38
13	Ne X Lyα	6.5	2.0–3.0	5.0–5.8	4.3	4.9	2.4
14	Fe XVII	6.6	2.1–2.6	5.5–5.7	4.2	1.3	18
15	Fe XVII	6.6	2.1–2.6	5.5–5.7	4.2	1.3	4.5
16	O VIII Lyα	6.9	1.6–2.6	4.6–5.7	3.8	4.3	100
17	O VII Heα	7.4	1.2–1.6	4.4–4.8	3.3	3.9	547
18	N VII Lyα	7.1	1.4–2.2	4.5–5.6	3.6	4.3	13

Notes.
[a] Characteristic LoS distance r_c, where the modeled AMD of the specific charge state becomes maximum (i.e., $\Delta N_{\rm H}/\Delta(\log\xi)$ is maximum). See the text for details.
[b] Range of ionization parameter ξ [erg cm s^{-1}] over which the local ionic column per ionization parameter bin is greater than 50% of the locally maximum ionic column.
[c] Range of temperature T [K] over which the local ionic column per ionization parameter bin is greater than 50% of the locally maximum ionic column.
[d] Characteristic number density n_c [cm^{-3}] of ion at $r = r_c$.
[e] LoS-integrated column $N_{\rm H}^{\rm tot}$ [$\times 10^{21}$ cm^{-2}] of ion.

ignored scattering that may fill in some of the line profiles (note that this would occur preferentially at the shorter wavelengths of the profiles, as the scattering depth is larger at smaller distances and the scattering cross section competes with that of photoabsorption). Finally, the breakdown of self-similarity near the axis at small radii and/or of the smoothness of the wind geometry may also contribute to this discrepancy. While beyond the scope of the current paper, we plan to address this issue quantitatively in a future work.

An important set of observations additional to those discussed herein have been those of Mehdipour et al. (2017), who analyzed the multiwavelength spectra of NGC 3783 during a recent, reduced soft X-ray ($E \lesssim 1$ keV) flux state in order to study the properties and physics of obscuring plasma in this AGN. They found that obscuration of the X-rays at $E \lesssim 1$ keV also produced more prominent Fe XXVI and Fe XXV absorption. They interpreted their results as due to the effects of an intervening, highly ionized obscurer. We defer detailed analysis of this latest data to a future publication. However, we would like to point out that within our framework, there may be a natural explanation, considering that an increased absorption column is due to increased poloidal mass flux. Such a view is supported by the fact that the optical and UV (O-UV) continua of their 2016 observations are a factor of $\simeq$2 higher than that of the early-2000s ones (the so-called "unobscured state") analyzed in the present paper (while their hard X-ray fluxes have so far remained unchanged). If the wind and disk mass fluxes vary in unison, as implicit in our model, the excess mass flux of the absorber (i.e., the wind) is then related to increased mass flux in the disk that drives the O-UV emission of this object. If the O-UV spectrum is emitted at radii larger than those of the X-rays (Chartas et al. 2009a; Kazanas 2015), and the excess mass is slowly being accreted inward, one should expect an increase in the X-ray flux to follow that of the O-UV, with a corresponding increase in soft X-ray ionization.

5.1. Mass Accretion for Disk Winds

Our wind model predicts that the wind mass flux scales with distance as $\dot{M}(x) \propto x^{3/2-p}$, where $x \equiv r/r_o \sim r/r_S$. This means that, for $p < 3/2$, the wind mass flux increases with distance; i.e., most of the mass available for accretion is lost into the wind at large distances from the black hole. This implies that the disk accretion rate should decrease toward the black hole. While our models do not address this problem, they have to allow for accretion onto the black hole at a rate sufficient to produce the observed bolometric luminosity. To provide an approximate resolution of this issue, we assume that the ratio of the wind mass flux to that of the disk is unity, $f_w \simeq 1$, independent of the radius (see F10a; Fukumura et al. 2017). In this way, we can connect the mass flux at the outer edge of the disk[9] to that producing the observed luminosity through accretion onto the black hole. This argument then implies

$$\dot{M}(x = x_{\rm max} \simeq 10^6) \sim 10^{3(3-2p)}\dot{M}(x = 1), \qquad (7)$$

where $\dot{M}(x = 1) \simeq n_o \sigma_T r_S \dot{M}_{\rm E}$ is given in terms of the wind density normalization n_o, with $\dot{M}_{\rm E} \equiv L_{\rm E}/c^2$ being the Eddington mass flux rate, $L_{\rm E}$ being the Eddington luminosity, and σ_T being the Thomson cross section. For our best-fit model with $p = 1.15$ and $n_{11} = 6.9$ and for a black hole mass

[9] This part of the wind may be viewed as the putative torus in the context of a unified torus scenario (e.g., Königl & Kartje 1994; Kazanas et al. 2012).

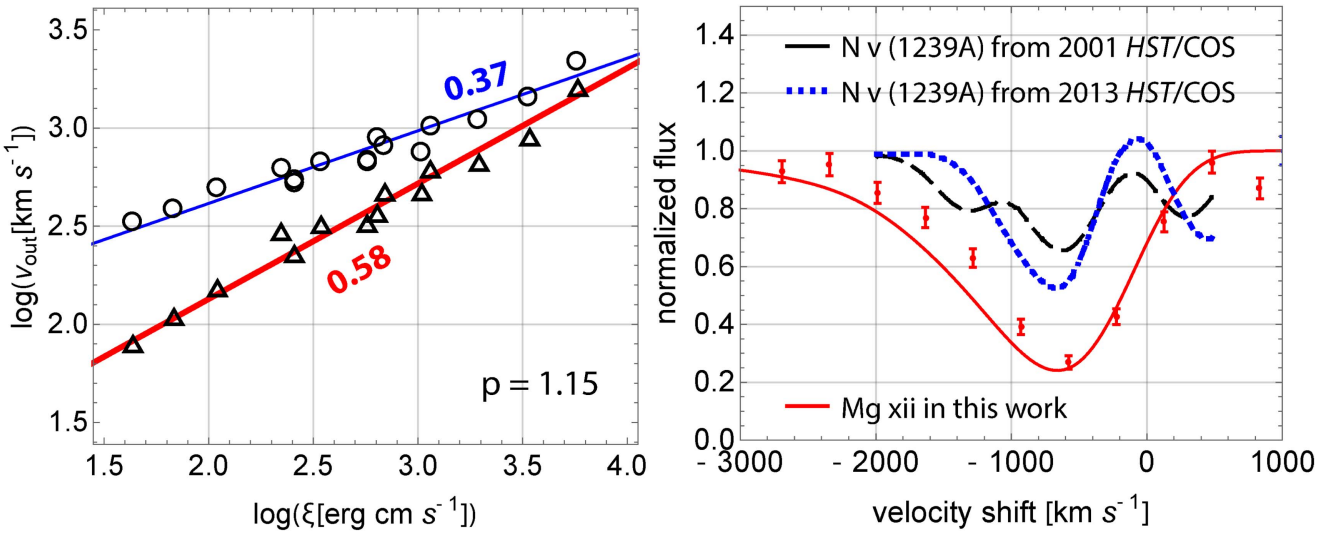

Figure 6. (a) Observed correlation between the LoS outflow speed $v_{\rm out}$ [km s^{-1}] and ionization parameter ξ [erg cm s^{-1}] for the 18 ions in Tables 2–3. Triangles denote a correlation with the velocity at which the ionic column derived from our model is locally maximum for each ion, while circles show a correlation for the same ions when the velocity is simply determined by the trough of the best-fit spectrum model for each ion in Figures 2–3. The blue line denotes the corresponding linear regression of slope 0.37 for the circles. Note that the predicted scaling (red line) from Equation (4), $v_{\rm out} \propto \xi^{1/\{2(2-p)\}} = \xi^{0.58}$ for $p = 1.15$, agrees very well with the best-fit correlation (triangles). (b) The solid red curve shows the normalized velocity profile of Mg XII Lyα (8.4192 Å) of the best-fit model $p = 1.15$ wind of this work. The dashed black and dotted blue curves represent the profiles of the UV N V absorber (1239 Å) from *HST*/COS 2001 and the 2013 observations in Scott et al. (2014), respectively. The UV spectra are intentionally smoothed to the velocity resolution ($\sim$100 km s^{-1}) of *Chandra*/HETG for comparison.

$M = 3 \times 10^7 M_\odot$, one obtains

$$\dot{M}(x \simeq 1) \sim 4\dot{M}_{\rm E} \simeq 1.8 \times 10^{27}\ {\rm g\ s^{-1}}, \quad (8)$$

$$\dot{M}(x_{\rm max} \simeq 10^6) \sim 500\dot{M}_{\rm E} \simeq 2.2 \times 10^{29}\ {\rm g\ s^{-1}}, \quad (9)$$

where $\dot{M}(x_{\rm max} \simeq 10^6)$ is available over an extended region ($x \lesssim 10^6$) of the disk to be provided for winds. Liberated accretion power via gravitational potential energy, given by $L \propto GM\dot{M}/r \propto x^{1/2-p}$, is more significant at smaller distances, contrary to the dominant mass accretion rate $\dot{M}$ at larger radii in Equation (7). Similarly, wind kinetic luminosity scales as

$$L_{\rm wind} \sim \dot{M} v_{\rm out}^2 \propto x^{1/2-p}, \quad (10)$$

and hence this power is very small ($\simeq 10^{-4}$) at $x_{\rm max} \simeq 10^6$ for $p = 1.15$, despite its large mass flux there, compared to that carried onto the black hole at $x \sim 1$. This fact has also been noted by Kraemer & Crenshaw (2012), which, using UV photonionization considerations for seven Seyfert galaxies, including NGC 3783, estimated that the UV absorber's mass flux is $\sim$100 times larger than what is needed to power the observed luminosity by accretion onto the black hole, consistent with our finding.

The best-fit value of $n_{11} = 6.9$ we have obtained implies a Thomson depth of order $\gtrsim$1 at the wind's innermost radius. For $f_w \simeq 1$, the corresponding accretion kinetic luminosity is $\sim 10^{46}$ erg s^{-1} (proportionally smaller for a smaller black hole mass), and, considering the efficiency of a Schwarzschild black hole ($\eta \simeq 0.05$, and maybe a little smaller if radiation is trapped in the flow), we obtain a bolometric luminosity of $\sim 5 \times 10^{44}$ erg s^{-1}. Considering its apportionment across the entire electromagnetic spectrum, the ionizing luminosity of $L_X \sim 3 \times 10^{43}$ erg s^{-1} employed in our modeling seems to be in reasonable agreement with the model's global mass flux budget and observations (see, e.g., Figure 6 in Mehdipour et al. 2017).

5.2. Physical Link: UV/X-Ray Absorbers and Narrow Line Region (NLR) Outflows

One of the open issues regarding AGN winds is the link between their X-ray absorbers and the known UV absorbers (e.g., C IV and N V) found in *HST*/COS/STIS observations (e.g., Crenshaw et al. 1999, 2003; Crenshaw & Kraemer 2012). Despite a number of analyses supporting this relation to date (Mathur et al. 1994, 1995; Crenshaw et al. 1999, 2003; Collinge et al. 2001; Kraemer et al. 2002; Krongold et al. 2003; Kaastra 2014), an explicit physical description of the underlying plasma dynamics is missing.

The simultaneous presence of *HST, Chandra*, and *XMM-Newton* in orbit has provided the opportunity of the synergistic study of absorbers in the X-ray and UV regions of the spectra of several AGNs. For example, Collinge et al. (2001) showed that the lower-ionization, X-ray Fe absorption features of NGC 4051 had corresponding UV counterparts, while the higher-ionization, higher-velocity X-ray absorbers of the spectrum lacked an equivalent UV absorption, indicating the absence of these ions in the higher-ionization, higher-velocity plasma. With respect to NGC 3783, Gabel et al. (2003) found the UV absorption features to have velocity structures similar to their X-ray counterparts, thereby arguing for the continuity of both absorption components.

In Figure 6(b), we show the data and our model profile of the Mg XII line (solid red) overlaid on the observed absorption lines of N V (dashed black for 2001 data and dotted blue for 2013 data) obtained by *HST*/COS data (from Scott et al. 2014; see their Figure 9) smoothed to the *Chandra*/HETG resolution ($\sim$100 km s^{-1}) for fair comparison. It is interesting that both the UV and X-ray lines exhibit approximately the same velocity structure (i.e., trough position and width) and absorption depth ($\tau_{\rm N\,V} \simeq 0.45$, $\tau_{\rm Mg\,XII} \simeq 1.5$), considering the difference in ionic

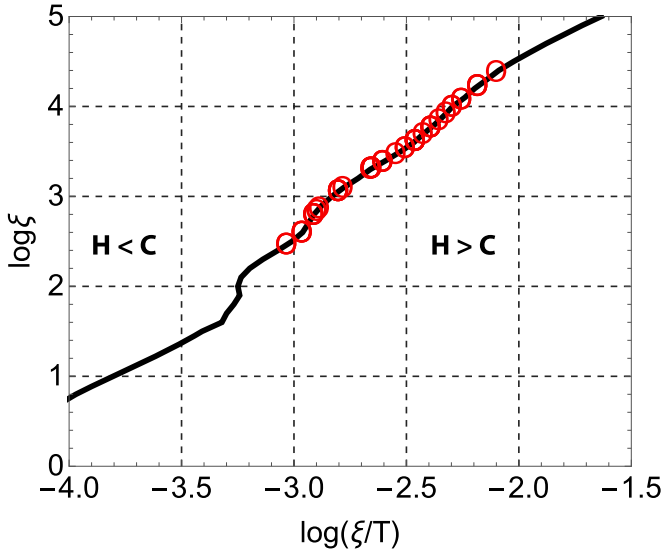

Figure 7. Modeled cooling curve (black) derived from the photoionization calculation with the best-fit wind solution of $p = 1.15$. Circles (red) indicate the positions of the 18 absorbers listed in Tables 2–3 in the parameter space. Regions where heating (H) or cooling (C) dominates are also indicated.

columns produced. It is noted that the 2001 UV N V line appears to exhibit a multiple trough feature. As discussed in Scott et al. (2014), it is conceivable that poorer spectral (velocity) resolution of X-ray measurements with *Chandra*/HETG may limit a detection of finer (smaller) kinematic components of X-ray absorbers. Nonetheless, the overall kinematic component seen in both UV (N V) and X-ray (Mg XII) observations looks surprisingly similar in depth and broadness in general. Since our model is focused primarily on X-ray winds, we will not discuss the UV absorbers any further. This would generally be an unlikely situation, because the two lines "live" in very different regions in ξ space (of $\log \xi \simeq 1$ for N V and $\log \xi \simeq 2$–3 for Mg XII) and the N V has a much higher absorption cross section. One could consider that their similar velocity structure argues for these ions belonging to the asymptotic velocity (and asymptotic ξ) region of a spherically symmetric wind whose mass flux can be arranged so that the ionic abundances of these two ions are roughly inversely proportional to their cross sections; this would produce similar line kinematics and depths. However, such a wind would preclude the presence of higher-ξ, higher-$v_{\rm out}$ ions such as Fe XXVI.

On the other hand, a UV/X-ray absorption-line similarity is possible within our model if we assume that the wind terminates at a distance r, or, equivalently, at an ionization parameter ξ, where N V is still subdominant, such that the ion abundances of these two ions are roughly inversely proportional to their cross section (since the N V column is smaller than that of Mg XII, these are only broad estimates). Then, their similar profiles will reflect the kinematic properties of this zone while maintaining roughly similar depths.

We have extended our X-ray ionization calculations to the UV ionization zone of N V to find a line absorption depth $\tau_{\rm N\,V} \simeq 0.35$ at $r/r_S \sim 10^6$ and $v_{\rm out} \sim 500$ km s^{-1}. The termination of the wind takes place in our model at a distance of $\sim$1 pc along the LoS. An extension of the (self-similar) wind to larger distances would result in a much lower N V velocity and high-absorption N V depth that are not observed. Finally, one additional consideration in comparing the O-UV and X-ray absorption-line profiles is that the UV source region is likely to be larger than that of the X-rays (Chartas et al. 2009a); therefore, their profiles do not necessarily correspond to the same LoS and velocity structures. Also, the UV source may not be totally covered by the wind if it is clumpy.

5.3. Clumpy Absorbers

An altogether different scenario to produce the observed AMD distribution is that of AGN clouds (clouds have been a basic staple of AGN phenomenology, especially since the work of Krolik et al. 1981) that are not uniform but include a density stratification (e.g., Gonçalves et al. 2006; Różańska et al. 2006; Stern et al. 2014; Adhikari et al. 2015; Goosmann et al. 2016). This alternative view is mostly prompted by the lack of some ions in the observed AMD over a finite narrow ionization parameter space; e.g., at $\log \sim$ 1–2 for IRAS 13349+2438 and NGC 3783 (e.g., Holczer et al. 2007) and $\log \xi \sim$ 2–2.8 for Mrk 509 (e.g., Detmers et al. 2011). Since clouds are thought to be the products of a thermal instability occurring in X-ray photoionized plasmas under constant pressure, the absence of transitions at specific ξ values is often attributed to this instability. While these considerations have not been incorporated in our calculations, we would like to mention that our winds operate under conditions of constant density (locally), a situation not conducive to the aforementioned instability (e.g., Różańska et al. 2006).

Figure 7 shows a calculated cooling curve for the best-fit photoionized wind of $p = 1.15$ under constant density thermal equilibrium; no thermal instability is apparent, typically indicated by a double-valued `S-shaped` region in $\xi - \Xi$ space, where $\Xi \equiv \xi/T$. The positions of the ions considered in this work (see Tables 2–3) are marked by the circles on the cooling curve at the derived values of ξ and T. Generally, under the thermal instability conditions, the observed ions should be associated with clouds in pressure equilibrium with hot gas. However, these occur under rather narrow regions in ξ inconsistent with the broad range of ionization values inferred from the observed transitions.

6. Summary

The line profiles of Figures 2–3 highlight the success of our theoretical approach to model MHD-driven absorbers. (1) The properties of individual lines (i.e., shape and EW) are not independent; they were all computed with the same (and also help define the) global parameters of a wind that spans 10^5–10^6 Schwarzschild radii in space, and hence their physical conditions are all mutually coupled. (2) The detailed profiles of the lines are not symmetric (as they would be if fit with Gaussians or Voigt functions); they are skewed blueward in wavelength, a feature due to the combined variation of ionic abundances with ξ (they decrease faster beyond their maximum value and more gradually prior to that; see the AMD in Figure 1) and the corresponding variation of the wind velocity with ξ, as expected in a continuous disk wind. The observed skewed profiles reflect this property, indicating that the velocity structure of the wind model is a reasonable representation of the real one. (3) The Fe XXV feature, usually a strong one in AGNs (Tombesi et al. 2013), is weak in NGC 3783. Our wind model reproduces the weakness of this line feature, in agreement with the observation.

In conclusion, the successful modeling of the absorbers of the AGN NGC 3783, along with those of the Galactic binary

GRO J1655-40 (Fukumura et al. 2017), with the same global model argues strongly for an underlying magnetized outflow of an invariant character not unlike that of our MHD model. It is found, very similarly to the analysis for GRO J1655-40, that the wind is magnetically launched and accelerated with a global density structure of $n(r) = 6.9 \times 10^{11}(r/r_o)^{-1.15}\,\mathrm{cm}^{-3}$ with a viewing angle of 44°.

We note also that the possibility of MHD-driving disk winds is independently discussed in the context of the Fe K UFOs in the well-studied Seyfert 1 AGN NGC 4151 by, e.g., Kraemer et al. (2018). Attributed to their typically high ionization parameter (e.g., $\log \xi \gtrsim 4.0$) and near-Compton thick column (e.g., $N_{\rm H} \sim 10^{23-24}\,\mathrm{cm}^{-2}$), magnetic origin seems to be a natural process, especially for the UFOs, as their study suggests. If a global magnetic field anchored to the underlying accretion disk is a generic component in AGNs/XRBs, then it is quite conceivable that the same magnetic field can play a significant role in launching the WAs discussed in this work for NGC 3783.

More detailed spectroscopic analyses of this kind will be made possible with the launch of *XARM* in the coming years and later by ESA's mission *Athena* through micro-calorimeter observations. These missions will be able to better constrain the otherwise very enigmatic absorption properties with an unprecedented statistical significance, perhaps leading to answering (partially if not fully) the ultimate question of launching mechanisms and the relations of the UV/X-ray absorbers seen in diverse AGNs.

We thank the anonymous referee for constructive comments and questions. K.F. is grateful to Steve Kraemer, Travis Fischer, and Patrick Hall for their insightful discussion on magnetically launched X-ray winds in AGNs. F.T. acknowledges support by the Programma per Giovani Ricercatori—anno 2014 "Rita Levi Montalcini." The research at the Technion is supported by the I-CORE program of the Planning and Budgeting Committee (grant number 1937/12). E.B. is grateful for the warm hospitality, support, and visiting professorship at the University of Maryland, College Park, and for funding from the European Union's Horizon 2020 research and innovation program under Marie Sklodowska-Curie grant agreement No. 655324. This work is supported in part by NASA/ADAP (NNH15ZDA001N-ADAP) and *Chandra* AO17 archival proposal grants.

ORCID iDs

Keigo Fukumura https://orcid.org/0000-0001-5709-7606
Demosthenes Kazanas https://orcid.org/0000-0002-7435-7809
Francesco Tombesi https://orcid.org/0000-0002-6562-8654
Ioannis Contopoulos https://orcid.org/0000-0001-6890-4143

References

Adhikari, T. P., Różańska, A., Sobolewska, M., & Czerny, B. 2015, ApJ, 815, 83
Alloin, D., Santos-Lleo, M., Peterson, B. M., et al. 1995, A&A, 293, 293
Begelman, M. C., McKee, C. F., & Shields, G. A. 1983, ApJ, 271, 70
Behar, E. 2009, ApJ, 703, 1346 (B09)
Behar, E., Rasmussen, A. P., Blustin, A. J., et al. 2003, ApJ, 598, 232
Blandford, R. D., & Payne, D. G. 1982, MNRAS, 199, 883 (BP82)
Blustin, A. J., Page, M. J., Fuerst, S. V., Branduardi-Raymont, G., & Ashton, C. E. 2005, A&A, 431, 111
Casse, F., & Ferreira, J. 2000a, A&A, 353, 1115
Casse, F., & Ferreira, J. 2000b, A&A, 361, 1178
Chakravorty, S., Petrucci, P.-O., Ferreira, J., et al. 2016, A&A, 589 119
Chartas, G., Kochanek, C. S., Dai, X., Pointdexter, S., & Garmire, G. P. 2009a, ApJ, 693, 174
Chartas, G., Saez, C., Brandt, W. N., Giustini, M., & Garmire, G. P. 2009b, ApJ, 706, 644
Collinge, M. J., Brandt, W. N., Kaspi, S., et al. 2001, ApJ, 557, 2
Contopoulos, I., Kazanas, D., & Fukumura, K. 2017, MNRAS, 472, 20
Contopoulos, J., & Lovelace, R. V. E. 1994, ApJ, 429, 139 (CL94)
Couto, J. D., Kraemer, S. B., Turner, T. J., & Crenshaw, D. M. 2016, ApJ, 833, 191
Crenshaw, D. M., & Kraemer, S. B. 2012, ApJ, 753, 75
Crenshaw, D. M., Kraemer, S. B., & George, I. M. 2003, ARA&A, 41, 117
Crenshaw, D. M., Kraemer, S. B., Boggess, A., et al. 1999, ApJ, 516, 750
Detmers, R. G., Kaastra, J. S., Steenbrugge, K. C., et al. 2011, A&A, 534, 38
Ferland, G. J., Porter, R. L., van Hoof, P. A. M., et al. 2013, RMxAA, 49, 137
Ferreira, J. 1997, A&A, 319, 340
Fiore, F., Elvis, M., Mathur, S., Wilkes, B. J., & McDowell, J. C. 1993, ApJ, 415, 129
Fukumura, K., Kazanas, D., Contopoulos, I., & Behar, E. 2010a, ApJ, 715, 636 (F10a)
Fukumura, K., Kazanas, D., Contopoulos, I., & Behar, E. 2010b, ApJL, 723, L228 (F10b)
Fukumura, K., Kazanas, D., Shrader, C. D., et al. 2017, NatAs, 1, 0062
Fukumura, K., Tombesi, F., Kazanas, D., et al. 2014, ApJ, 780, 120
Fukumura, K., Tombesi, F., Kazanas, D., et al. 2015, ApJ, 805, 17
Gabel, J. R., Crenshaw, D. M., Kraemer, S. B., et al. 2003, ApJ, 583, 178
Gabel, J. R., Kraemer, S. B., Crenshaw, D. M., et al. 2005, ApJ, 631, 741
George, I. M., Turner, T. J., Netzer, H., et al. 1998, ApJS, 114, 73
Gofford, J., Reeves, J. N., McLaughlin, D. E., et al. 2015, MNRAS, 451 4169
Gonçalves, A. C., Collin, S., Dumont, A.-M., et al. 2006, A&A, 451, 23
Goosmann, R. W., Holczer, T., Mouchet, M., et al. 2016, A&A, 589, 76
Gupta, A., Mathur, S., & Krongold, Y. 2015, ApJ, 798, 4
Halpern, J. P. 1984, ApJ, 287, 90
Holczer, T., Behar, E., & Kaspi, S. 2007, ApJ, 663, 799
Kaastra, J. S. 2014, Sci, 345, 64
Kallman, T., & Bautista, M. 2001, ApJS, 133, 221
Kallman, T. R., Bautista, M. A., Goriely, S., et al. 2009, ApJ, 701, 865
Kaspi, S., Brandt, W. N., George, I. M., et al. 2002, ApJ, 574, 643 (K02)
Kaspi, S., Brandt, W. N., Netzer, H., et al. 2000, ApJ, 535, 17
Kaspi, S., Brandt, W. N., Netzer, H., et al. 2001, ApJ, 554, 261 (K01)
Kazanas, D. 2015, ASSL, 414, 207
Kazanas, D., Fukumura, K., Contopoulos, I., Behar, E., & Shrader, C. R. 2012, AstRv, 7, 92
Köngl, A., & Kartje, J. F. 1994, ApJ, 434, 446
Kraemer, S. B., & Crenshaw, D. M. 2012, ApJ, 753, 75
Kraemer, S. B., Crenshaw, D. M., & Gabel, J. R. 2001, ApJ, 557, 30
Kraemer, S. B., Crenshaw, D. M., George, I. M., et al. 2002, ApJ, 577, 98
Kraemer, S. B., Tombesi, F., & Bottorff, M. C. 2018, ApJ, 852, 35
Krolik, J. H., McKee, C. F., & Tarter, C. B. 1981, ApJ, 249, 422
Krongold, Y., Nicastro, F., Brickhouse, N. S., et al. 2003, ApJ, 597, 832
Laha, S., Guainazzi, M., Dewangan, G. C., Chakravorty, S., & Kembhavi, A. K. 2014, MNRAS, 441, 2613
Luketic, S., Proga, D., Kallman, T. R., Raymond, J. C., & Miller, J. M. 2010, ApJ, 719, 515
Mathur, S., Elvis, M., & Wilkes, B. 1995, ApJ, 452, 230
Mathur, S., Wilkes, B., Elvis, M., & Fiore, F. 1994, ApJ, 434, 493
McKernan, B., Yaqoob, T., & Reynolds, C. S. 2007, MNRAS, 379, 1359
Mehdipour, M., Kaastra, J. S., Kriss, G. A., et al. 2017, A&A, in press (arXiv:1707.04671)
Miller, J. M., Fabian, A. C., Kaastra, J., et al. 2015, ApJ, 814, 87
Miller, J. M., Raymond, J., Fabian, A., et al. 2006, Natur, 441, 953
Miller, J. M., Raymond, J., Reynolds, C. S., et al. 2008, ApJ, 680, 1359
Murray, N., Chiang, J., Grossman, S. A., & Voit, G. M. 1995, ApJ, 451 498
Nandra, K., & Pounds, K. A. 1992, Natur, 359, 215
Nandra, K., Fabian, A. C., George, I. M., et al. 1993, MNRAS, 260, 504
Netzer, H., Kaspi, S., Behar, E., et al. 2003, ApJ, 599, 933
Peterson, B. M., Ferrarese, L., Gilbert, K. M., et al. 2004, ApJ, 613, 682
Proga, D., Stone, J. M., & Kallman, T. R. 2000, ApJ, 543, 686
Reeves, J. N., Nandra, K., George, I. M., et al. 2004, ApJ, 602, 648
Reeves, J. N., O'Brien, P. T., Braito, V., et al. 2009, ApJ, 701, 493
Reynolds, C. S., Fabian, A. C., Nandra, K., et al. 1995, MNRAS, 277, 901

Reynolds, C. S., Ward, M. J., Fabian, A. C., & Celotti, A. 1997, MNRAS, 291, 403
Różańska, A., Goosmann, R., Dumont, A.-M., & Czerny, B. 2006, A&A, 452, 1
Scott, A. E., Brandt, W. N., Behar, E., et al. 2014, ApJ, 797, 105
Steenbrugge, K. C., Kaastra, J. S., Crenshaw, D. M., et al. 2005, A&A, 434, 569
Stern, J., Behar, E., Laor, A., Baskin, A., & Holczer, T. 2014, MNRAS, 445, 3011
Tombesi, F., Cappi, M., Reeves, J. N., et al. 2010, A&A, 521, 57
Tombesi, F., Cappi, M., Reeves, J. N., et al. 2013, MNRAS, 430 1102
Tombesi, F., Meléndez, M., Veilleux, S., et al. 2015, Natur, 519 436
Turner, T. J., Kraemer, S. B., George, I. M., Reeves, J. N., & Bottorff, M. C. 2005, ApJ, 618, 155
Turner, T. J., Nandra, K., George, I. M., Fabian, A. C., & Pounds, K. A. 1993, ApJ, 419, 127